

6

IMPLEMENTATION AND VALIDATION OF LES/FGM METHOD IN OPENFOAM

This chapter reports the implementation and validation of the FGM method in the framework of OpenFOAM®. A methane/air jet in vitiated coflow flame that shares many common features with the DSHC case H_{II} is used as test case. Parameter studies using an Unsteady Reynolds Averaged Navier Stokes (URANS) technique, reveal that the auto-ignition process is highly sensitive to the model constants in the transport equations for the mixture fraction and progress variable variances. To overcome the uncertainties on the model constants choice, dynamic procedures are proposed in the context of Large Eddy Simulation (LES). A significant improvement on the prediction of the considered case is achieved with the dynamic model.

6.1. INTRODUCTION

The auto-ignition process is an important phenomenon of great practical interest, e.g. in Homogeneous Charge Compression Ignition (HCCI) or Premixed Charge Compression Ignition (PCCI) engines. However, a correct prediction of the auto-ignition process in flowing media is very difficult, because, the turbulent-chemistry interaction (TCI) plays an crucial role in it. Many studies already investigated this process with different computational approaches [1–4]. In this paper, we focus on the role of TCI in auto-ignition modeling when tabulated chemistry model is employed for combustion.

The auto-ignition process in hydrogen and low hydrocarbon flames is recognized as an accumulation of hydroperoxyl (HO_2) upstream of the flame base, followed by considerable heat release and accumulation of hydroxyl (OH). To correctly capture the auto-ignition process, a detailed chemical mechanism must be incorporated in the simulation. However, a direct use of a detailed chemical mechanism, as can be done with for example the transported PDF method or the Eddy Dissipation Concept model, not only significantly increases the computational cost, but also brings in extra numerical difficulties due to the strong stiffness of the chemical reaction system. Proper chemistry reduction is required for affordable yet accurate simulations. This is accomplished by either using reduced chemical mechanisms, or employing tabulated chemistry methods [5]. In this study the Flamelet Generated Manifolds model [6] is used, which is a tabulated chemistry method.

The FGM model builts on the flamelet concept [7] and combines it with a manifold approach [6]. The multi-dimensional turbulent flame is considered as a set of 1D flamelets. A low dimensional manifold that is capable of describing the mixing, reaction and other major processes or properties of the turbulent flame is then constructed based on the laminar flamelets calculation. In the turbulent flame simulation, only the transport equations of the controlling variables in addition to the continuity and momentum conservation equations are solved. In this way the costly chemical reaction process is decoupled from the main simulation, and therefore the FGM method is computationally very efficient.

When this tabulated chemistry method is applied, the TCI is accounted for normally by the probability density function (PDF) of the controlling parameters, e.g. mixture fraction and progress variable. The Artificially thickened flame (ATF) model can also be combined with FGM [8], however this is out of the scope of the current work. The PDFs can be obtained by solving modeled transport equations for the joint PDFs [9, 10]. But it is more common to simply assume that they obey a certain shape which can be determined by the first and second moments of the controlling parameters. Mean values of the controlling parameters, in most cases, are obtained by solving transport equations. To obtain the values for the second moments, namely the variances and possibly also co-variances, of the controlling parameters both a transport equation model and an algebraic model, have been used. LES simulations of Sandia Flames D and F performed by Vreman et al. [11] using the FGM model found that the inclusion of modeled subfilter variances of mixture fraction and progress variable as additional entries to the manifold had only small effects on the simulation of both Sandia Flame D and F. However, a LES study by Ihme and See [12] on a lifted methane/air jet flame showed that including or not the Sub-Grid Scale (SGS) variance of progress variable has a significant influence on the

predicted flame lift-off height. The seemingly contradictory conclusions are suggesting that the role of scalar variances on combustion modeling deserves careful investigation. Therefore, influence of the models for the mixture fraction and progress variable variances on the auto-ignition process is the focus of this study.

The lifted methane/air jet flame experimentally studied by Cabra et al [13] is chosen as a target flame. Gordon et al [1] modeled this flame with the transported composition PDF approach. By analyzing the transport budget and qualitative behavior of key species such as HO_2 , they concluded that the stabilization of this flame is primarily controlled by auto-ignition, for which the TCI is important. Therefore this flame is a suitable validation case for this study. Ihme and See [12] investigated this flame by Large Eddy Simulation (LES) using the unsteady flamelet/progress variable model. Other studies on this flame can be found in the references of [12].

To handle the wide time and length scale range in turbulence and combustion, three levels of simulation exist: direct numerical simulation (DNS), large eddy simulation (LES) and Reynolds-Averaged Navier Stokes (RANS) simulation, with increasing extent of modeling requirement. Due to the enormous computational resources needed for DNS, its application is still limited to academic research. RANS has for long been the workhorse for industrial application, while LES is gradually entering this field. With this in mind, we will study the auto-ignition process using both unsteady RANS (URANS) and LES techniques. As stated in [12], the intermittent ignition events typically occur on scales that are computationally not resolved in LES. Therefore in LES, the SGS TCI still deserves careful investigation. The FGM model has been implemented by the authors in the open source CFD package OpenFoam [14], and the simulation of this study is carried out using this newly developed OpenFoam FGM solver.

The present research makes contributions in the following three ways: first, an advanced combustion model (FGM) and related sub-models were implemented in the open source CFD package OpenFOAM and validated in this paper. Second, new dynamic models for SGS variances of FGM controlling parameters are proposed, promising performance of which is demonstrated. Last but not least, both URANS and LES have been used for the simulation, making possible the comparison of the capability and limitation of each approach. The rest of the paper is structured as follows: the mathematical modeling approach for the FGM method is presented in section 6.2, followed by a detailed explanation on the turbulence modeling. In section 6.4, models for the FGM controlling parameters variances are discussed, especially dynamic procedures for calculating the SGS scalar variances are developed. Details of the numerical solver adopted are given in section 6.5 before the analysis of the results in section 6.6. Main conclusions are summarized in the last section.

6.2. MATHEMATICAL MODELING

6.2.1. FLAMELET GENERATED MANIFOLDS

Instead of directly solving the transport equations for each species, a tabulated chemistry method – the Flamelet Generated Manifolds model [6] – is used in this study. Neglecting the effect of radiative heat transfer, in this FGM approach, the scalars, such as temperature, species mass fractions, density or source term, are stored in the lookup ta-

ble as function of the mixture fraction and the progress variable. Mixture fraction quantifies the extent of mixing between fuel and oxidizer streams in non-premixed combustion. Bilger's formula is adopted here [15]:

$$Z = \frac{b - b_o}{b_f - b_o}, \quad (6.1)$$

where $b = 2 \frac{Y_C}{W_C} + 0.5 \frac{Y_H}{W_H} - \frac{Y_O}{W_O}$ for hydrocarbon fuels. Subscripts C, H and O correspond to the elements C, H and O, respectively. And subscripts o and f refer to the oxidizer and the fuel stream conditions, respectively. Progress variable C is a parameter that characterizes the evolution of "global" chemical status from purely mixing ($C = 0$) to "fully burnt" ($C = 1$). In this way, the high-dimensional chemical reaction system has been projected to a two dimensional manifold:

$$\phi = \phi(Z, C), \quad (6.2)$$

where ϕ can be any of the scalar properties of this system. This two dimensional manifold is referred in the following as the FGM table. In this study, the FGM table is created by solving laminar counterflow diffusion flame at different strain rate in physical space and then transfer the results to mixture fraction and progress variable space.

DEFINITION OF PROGRESS VARIABLE

A progress variable is generally defined as a linear combination of species mass fractions.

6

$$Y_c = \sum_{k=1}^N w_k Y_k, \quad (6.3)$$

where w is the weight factor and Y_k is the mass fraction for k -th species, followed by normalisation

$$C = \frac{Y_c - Y_c^u}{Y_c^b - Y_c^u}, \quad (6.4)$$

where the superscripts b and u respectively represent the burnt and unburnt status. To avoid confusion, in this paper we refer Y_c as progress variable and C as scaled progress variable. A transport equation has to be solved for either progress variable or scaled progress variable. It is more convenient to solve for the unscaled progress variable Y_c , since this avoids the necessity of modeling extra source terms appearing in the transport equation of scaled progress variable C .

In the present study the following definition of progress variable is used:

$$Y_c = a \frac{Y_{H_2O}}{W_{H_2O}} + b \frac{Y_{CO_2}}{W_{CO_2}} + c \frac{Y_{H_2}}{W_{H_2}} + d \frac{Y_{CO}}{W_{CO}}. \quad (6.5)$$

After a parameter study, the progress variable with $a = 4$, $b = 2$, $c = 1/2$ and $d = 1$ has been selected in this study. Since the species involved in the definition of progress variable are experimentally measured, scatter plots of temperature and CH_4 mass fraction are shown as functions of two different definitions of progress variable in Fig. 6.1. The same quantities retrieved from the FGM tables are also plotted for comparison. First of all, it can be clearly seen that the change of measured temperature and Y_{CH_4}

with progress variable are well represented by the FGM table. Second, the progress variable that is employing the information of CO and H₂ can also represent the reaction at the rich region. Taking mass fraction of CH₄ as example, in the case of $Y_c = Y_{CO_2}/M_{CO_2} + Y_{H_2O}/M_{H_2O}$ the mass fraction of CH₄ drops almost vertically at a constant progress variable (around $Y_c = 8$) for high mixture fraction, meaning the reaction for rich mixture can not be indicated by this progress variable. With the second definition of progress variable, the consumption of CH₄ for both rich and lean mixture are well represented. A similar observation can also be made from the plot of CO₂ mass fraction (not shown here). With the progress variable used in this study, both temperature and Y_{CH_4} change monotonically with respect to progress variable, at fixed mixture fraction.

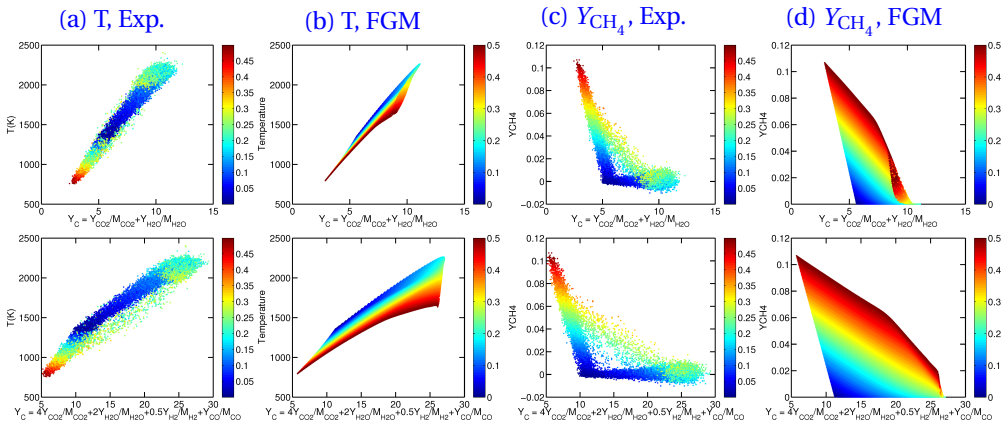


Figure 6.1: Scatter plots in $Y_c - T$ and $Y_c - Y_{CH_4}$ space, colored by mixture fraction.

PRESUMED PDF METHOD

The influence of turbulent fluctuations on the local flame structure is accounted for through the joint PDF of the independent variables. The Favre-averaged/filtered scalars are calculated as:

$$\bar{\phi} = \int_0^1 \int_0^1 \phi(Z, C) \tilde{P}(Z, C) dZ dC. \quad (6.6)$$

The Reynolds-averaged/filtered mean of scalar $\bar{\phi}$ and density $\bar{\rho}$ can be computed as follows:

$$\bar{\phi} = \bar{\rho} \int_0^1 \frac{\phi(Z, C)}{\rho(Z, C)} \tilde{P}(Z, C) dZ dC, \quad (6.7)$$

and

$$\bar{\rho} = \left[\int_0^1 \frac{\tilde{P}(Z, C)}{\rho(Z, C)} dZ dC \right]^{-1}, \quad (6.8)$$

where $\tilde{P}(Z, C)$ is the joint PDF of mixture fraction and scaled progress variable. It is possible to directly calculate the joint PDFs with transported PDF method, which eliminates any assumption on the shape of the joint PDFs. Such a combined FGM / transported PDF method has been used by the authors for the simulation of a spray jet flame [10].

Alternatively, a presumed PDF method can be adopted, in which the PDFs are assumed to obey a certain shape which can be determined by the first and second moments of the controlling parameters. In this study the latter approach, namely the FGM / presumed PDF method is used. It is a common practice to assume that Z and C are statistically independent of each other, namely

$$\tilde{P}(Z, C) = \tilde{P}(Z)\tilde{P}(C). \quad (6.9)$$

β -function is widely accepted as a good representation of the PDF of mixture fraction. The β -function PDF is defined as:

$$\tilde{P}(\phi) = \frac{\tilde{\phi}^{\alpha-1}(1-\tilde{\phi})^{\beta-1}\Gamma(\alpha+\beta)}{\Gamma(\alpha)\Gamma(\beta)}, \quad (6.10)$$

where the shape parameters α and β are determined by mean and variance of scalar ϕ .

$$\alpha = \tilde{\phi} \left[\frac{\tilde{\phi}(1-\tilde{\phi})}{\tilde{\phi}''/2} - 1 \right], \quad (6.11)$$

$$\beta = (1-\tilde{\phi}) \frac{\alpha}{\tilde{\phi}}. \quad (6.12)$$

Both δ -function and β -function have been used as PDF of progress variable [16, 17]. The fluctuation of progress variable has been proven to be important for the target flame [12], so the β -function is also adopted for progress variable in the present study.

As can be seen from Eqs. (6.10) to (6.12), the mean and variance of mixture fraction and progress variable are required to obtain the PDFs. The mean value of mixture fraction is obtained by solving its transport equation:

$$\frac{\partial \bar{\rho} \tilde{Z}}{\partial t} + \frac{\partial \bar{\rho} \tilde{u}_j \tilde{Z}}{\partial x_j} = \frac{\partial}{\partial x_j} \left(\bar{\rho} \tilde{D} \frac{\partial \tilde{Z}}{\partial x_j} - \Phi_{Z,j} \right). \quad (6.13)$$

And the mean value of scaled progress variable, \tilde{C} , is obtained by firstly solving transport equation for \tilde{Y}_c and then converting \tilde{Y}_c to \tilde{C} . The transport equation for \tilde{Y}_c reads:

$$\frac{\partial \bar{\rho} \tilde{Y}_c}{\partial t} + \frac{\partial \bar{\rho} \tilde{u}_j \tilde{Y}_c}{\partial x_j} = \frac{\partial}{\partial x_j} \left(\bar{\rho} \tilde{D} \frac{\partial \tilde{Y}_c}{\partial x_j} - \Phi_{Y_c,j} \right) + \bar{\omega}_{Y_c}. \quad (6.14)$$

\tilde{Y}_c can be converted to \tilde{C} by:

$$\tilde{C} = \frac{\tilde{Y}_c - \tilde{Y}_c^u}{\tilde{Y}_c^b - \tilde{Y}_c^u}, \quad (6.15)$$

where \tilde{Y}_c^u and \tilde{Y}_c^b are respectively the pdf-integrated minimum and maximum value of progress variable.

In Eqs. (6.13) and (6.14), there are several unclosed terms: SGS/turbulence fluxes for mixture fraction and progress variable, Φ_Z and Φ_{Y_c} , and the mean source term for

progress variable $\bar{\omega}_{Y_c}$. The SGS turbulence fluxes for mixture fraction and progress variable are modeled with the standard gradient diffusion assumption:

$$\Phi_{Z,j} = -\bar{\rho} D_t \frac{\partial \tilde{Z}}{\partial x_j} = -\bar{\rho} \frac{\nu_t}{Sc_t} \frac{\partial \tilde{Z}}{\partial x_j}, \quad (6.16)$$

$$\Phi_{Y_c,j} = -\bar{\rho} D_t \frac{\partial \tilde{Y}_c}{\partial x_j} = -\bar{\rho} \frac{\nu_t}{Sc_t} \frac{\partial \tilde{Y}_c}{\partial x_j}, \quad (6.17)$$

where D_t is the turbulent diffusivity, μ_t is the turbulent viscosity, which will be discussed in Section 6.3. Sc_t is the turbulent Schmidt number, which was set to 0.7 in both the URANS and LES cases in this study.

Transport equations for the variances of mixture fraction and progress variable can be derived from the exact and averaged/filtered transport equations of mixture fraction and progress variable, making use of the continuity equation (see 6.7):

$$\frac{\partial \bar{\rho} \tilde{Z}''^2}{\partial t} + \frac{\partial \bar{\rho} \tilde{u}_j \tilde{Z}''^2}{\partial x_j} = \frac{\partial}{\partial x_j} \left(\bar{\rho} D \frac{\partial \tilde{Z}''^2}{\partial x_j} - \Phi_{Z_v,j} \right) - 2\bar{\rho} \tilde{s}_{\chi_Z} - 2\Phi_{Z,j} \frac{\partial \tilde{Z}}{\partial x_j}, \quad (6.18)$$

$$\begin{aligned} \frac{\partial \bar{\rho} \tilde{Y}_c''^2}{\partial t} + \frac{\partial \bar{\rho} \tilde{u}_j \tilde{Y}_c''^2}{\partial x_j} &= \frac{\partial}{\partial x_j} \left(\bar{\rho} D \frac{\partial \tilde{Y}_c''^2}{\partial x_j} - \Phi_{Y_c,v,j} \right) - 2\bar{\rho} \tilde{s}_{\chi_{Y_c}} - 2\Phi_{Y_c,j} \frac{\partial \tilde{Y}_c}{\partial x_j} \\ &\quad + 2 \left(\overline{Y_c \dot{\omega}_{Y_c}} - \tilde{Y}_c \bar{\omega}_{Y_c} \right). \end{aligned} \quad (6.19)$$

In Eqs.(6.18) and (6.19), the SGS/turbulent fluxes of mixture fraction and progress variable variances, $\Phi_{Z_v,j}$ and $\Phi_{Y_c,v,j}$ are modeled with the Daly-Harlow generalized gradient diffusion model:

$$\Phi_{Z_v,j} = -\bar{\rho} D_t \frac{\partial \tilde{Z}''^2}{\partial x_j} = -\bar{\rho} \frac{\nu_t}{Sc_t} \frac{\partial \tilde{Z}''^2}{\partial x_j}, \quad (6.20)$$

$$\Phi_{Y_c,v,j} = -\bar{\rho} D_t \frac{\partial \tilde{Y}_c''^2}{\partial x_j} = -\bar{\rho} \frac{\nu_t}{Sc_t} \frac{\partial \tilde{Y}_c''^2}{\partial x_j}. \quad (6.21)$$

Conversion of $\tilde{Y}_c''^2$ to \tilde{C}''^2 can be done using:

$$\tilde{C}''^2 = \frac{\tilde{Y}_c''^2 - (\tilde{Y}_c)^2 - (\tilde{Y}_c^u)^2 - 2\tilde{C} \left[\tilde{Y}_c^u \tilde{Y}_c^b - (\tilde{Y}_c^u)^2 \right]}{\left(\tilde{Y}_c^b - \tilde{Y}_c^u \right)^2} - \tilde{C}^2, \quad (6.22)$$

where $(\tilde{Y}_c)^2$ and $\tilde{Y}_c^u \tilde{Y}_c^b$ were pdf-integrated and tabulated as functions of mean mixture fraction \tilde{Z} and its variance \tilde{Z}''^2 [18].

The unclosed terms in the transport equations of the mean and variance of mixture fraction and progress variable and their closure models are listed in Table 6.1.

Note that, Z and Y_c are in general not statistically independent, whereas Z and C come close to being statistically independent. We use \tilde{Z} and \tilde{C} as controlling parameters for tabulation. In the simulation, we solve transport equation for \tilde{Y}_c and convert it to \tilde{C} by relation (6.4) before table lookup. The range of variance depends on the mean

Table 6.1: Unclosed terms in RANS/LES transport equations for FGM controlling parameters

		RANS	LES	
Terms	Expression	Model	Expression	Model
$\Phi_{Z,j}$	$\bar{\rho} \widetilde{Z'' u_j''}$	Eq. (6.16)	$\bar{\rho} (\widetilde{Z u_j} - \tilde{Z} \tilde{u}_j)$	Eq. (6.16)
$\Phi_{Y_c,j}$	$\bar{\rho} \widetilde{Y_c'' u_j''}$	Eq. (6.17)	$\bar{\rho} (\widetilde{Y_c u_j} - \tilde{Y}_c \tilde{u}_j)$	Eq. (6.17)
$\Phi_{Z_v,j}$	$\bar{\rho} \widetilde{Z''^2 u_j''}$	Eq. (6.20)	$\Phi_{Z^2,j} - 2\tilde{Z}\Phi_{Z,j}$	Eq. (6.20)
$\Phi_{Y_c,j}$	$\bar{\rho} Y_c''^2 u_j''$	Eq. (6.21)	$\Phi_{Y_c^2,j} - 2\tilde{Y}_c \Phi_{Y_c,j}$	Eq. (6.21)
$\rho \tilde{s}_{\chi_Z}$	$\bar{\rho} \tilde{\chi}_Z - \bar{\rho} \tilde{D} \left(\frac{\partial \tilde{Z}}{\partial x_j} \right)^2$	Eq. (6.39)	$\bar{\rho} \tilde{\chi}_Z - \bar{\rho} \tilde{D} \left(\frac{\partial \tilde{Z}}{\partial x_j} \right)^2$	Eq. (6.41)
$\rho \tilde{s}_{\chi_{Y_c}}$	$\bar{\rho} \tilde{\chi}_{Y_c} - \bar{\rho} \tilde{D} \left(\frac{\partial \tilde{Y}_c}{\partial x_j} \right)^2$	Eq. (6.40)	$\bar{\rho} \tilde{\chi}_{Y_c} - \bar{\rho} \tilde{D} \left(\frac{\partial \tilde{Y}_c}{\partial x_j} \right)^2$	Eq. (6.42)
$\dot{\omega}_{Y_c}$	$\dot{\omega}_{Y_c}$	Tabulated	$\dot{\omega}_{Y_c}$	Tabulated
$\overline{Y_c \dot{\omega}_{Y_c}}$	$\overline{Y_c \dot{\omega}_{Y_c}}$	Tabulated	$\overline{Y_c \dot{\omega}_{Y_c}}$	Tabulated

value, therefore to simplify the table construction, the scaled variances of mixture fraction and progress variable $\tilde{\zeta}_Z$ and $\tilde{\zeta}_C$ are used as controlling parameters in the lookup table. They are related to variances of mixture fraction and process variable by the following expressions:

$$\tilde{\zeta}_Z = \frac{\widetilde{Z''^2}}{\tilde{Z}(1-\tilde{Z})}, \quad (6.23)$$

$$\tilde{\zeta}_C = \frac{\widetilde{C''^2}}{\tilde{C}(1-\tilde{C})}. \quad (6.24)$$

Table 6.2: Relations between lookup table controlling parameters and parameters solved in simulation

Table controlling parameters		Parameters solved		Conversion
Parameter	Range	Parameter	Range	
\tilde{Z}	[0,1]	\tilde{Z}	[0,1]	
\tilde{C}	[0,1]	\tilde{Y}_c	$[\tilde{Y}_c^u, \tilde{Y}_c^b]$	Eq. (6.15)
$\tilde{\zeta}_Z$	[0,1]	$\widetilde{Z''^2}$	$[0, \tilde{Z}(1-\tilde{Z})]$	Eq. (6.23)
$\tilde{\zeta}_C$	[0,1]	$\widetilde{Y}_c''^2$		Eqs. (6.22)
		$\widetilde{C''^2}$	$[0, \tilde{C}(1-\tilde{C})]$	Eqs. (6.24)

The FGM table controlling parameters and parameters solved in simulation as well as their conversion are summarized in Table 6.2.

6.2.2. MODELED GOVERNING EQUATIONS

Summarizing the discussions given above, and substituting the unclosed terms with their corresponding models, the modeled (URANS or LES) transport equations for tur-

bulent combustion using FGM/presumed PDF method can be expressed as follows:

$$\frac{\partial \bar{\rho}}{\partial t} + \frac{\partial \bar{\rho} \tilde{u}_j}{\partial x_j} = 0, \quad (6.25)$$

$$\frac{\partial \bar{\rho} \tilde{u}_i}{\partial t} + \frac{\partial (\bar{\rho} \tilde{u}_i \tilde{u}_j)}{\partial x_j} = -\frac{\partial \bar{p}}{\partial x_i} + \frac{\partial}{\partial x_j} \left(\bar{\mu} \tilde{S}_{ij}^D - R_{ij} \right), \quad (6.26)$$

$$\frac{\partial \bar{\rho} \tilde{Z}}{\partial t} + \frac{\partial \bar{\rho} \tilde{u}_j \tilde{Z}}{\partial x_j} = \frac{\partial}{\partial x_j} \left[\bar{\rho} (\tilde{D} + D_t) \frac{\partial \tilde{Z}}{\partial x_j} \right], \quad (6.27)$$

$$\frac{\partial \bar{\rho} \tilde{Y}_c}{\partial t} + \frac{\partial \bar{\rho} \tilde{u}_j \tilde{Y}_c}{\partial x_j} = \frac{\partial}{\partial x_j} \left[\bar{\rho} (\tilde{D} + D_t) \frac{\partial \tilde{Y}_c}{\partial x_j} \right] + \bar{\omega}_{Y_c}, \quad (6.28)$$

$$\frac{\partial \bar{\rho} \widetilde{Z''^2}}{\partial t} + \frac{\partial \bar{\rho} \tilde{u}_j \widetilde{Z''^2}}{\partial x_j} = \frac{\partial}{\partial x_j} \left[\bar{\rho} (\tilde{D} + D_t) \frac{\partial \widetilde{Z''^2}}{\partial x_j} \right] + C_g \bar{\rho} D_t \left(\frac{\partial \tilde{Z}}{\partial x_j} \right)^2 - C_{d,Zv} \bar{\rho} \tilde{s}_{\chi_Z}, \quad (6.29)$$

$$\frac{\partial \bar{\rho} \widetilde{Y_c''^2}}{\partial t} + \frac{\partial \bar{\rho} \tilde{u}_j \widetilde{Y_c''^2}}{\partial x_j} = \frac{\partial}{\partial x_j} \left[\bar{\rho} (\tilde{D} + D_t) \frac{\partial \widetilde{Y_c''^2}}{\partial x_j} \right] + C_g \bar{\rho} D_t \left(\frac{\partial \tilde{Y}_c}{\partial x_j} \right)^2 - C_{d,Y_cv} \bar{\rho} \tilde{s}_{\chi_{Y_c}} + 2 \left(\overline{Y_c \dot{\omega}_{Y_c}} - \tilde{Y}_c \bar{\omega}_{Y_c} \right), \quad (6.30)$$

$$S_{ij} = \frac{1}{2} \left(\frac{\partial u_i}{\partial x_j} + \frac{\partial u_j}{\partial x_i} \right), \quad (6.31)$$

where $S_{ij}^D = (S_{ij} - \frac{1}{3} \delta_{ij} S_{kk})$ is the deviatoric part of the strain rate tensor S_{ij} . R_{ij} is the Reynolds stress (in URANS) or sub-grid scale (SGS) stress (in LES). C_g , $C_{d,Zv}$ and C_{d,Y_cv} are model constants for the generation and dissipation terms of mixture fraction and progress variable variances respectively. C_g in fact is not really a free model constant since a theoretical value 2 is found in the derivation of the exact transport equation, and this value is adopted here. A wide range of values for $C_{d,Zv}$ from 1 to 16 have been reported in literatures for different cases [8, 19]. However, as will be shown in section 6.6, the auto-ignition process is very sensitive to these two constants, and a dynamic procedure for determining these two constants is developed in this paper.

In Eqs. (6.25) to (6.30), the Reynolds/SGS stresses, R_{ij} , and turbulent/SGS scalar dissipation rate, $\bar{\rho} \tilde{s}_{\chi_Z}$ and $\bar{\rho} \tilde{s}_{\chi_{Y_c}}$ remain unclosed. Models for these terms will be discussed in following sections.

6.3. TURBULENCE MODELING

In this section we discuss the turbulence models that are used to close the Reynolds/SGS stresses R_{ij} in the Eq. (6.26). To calculate the Reynolds stress in URANS the $k - \epsilon$ model is used. A modified model constant $C_{1\epsilon} = 1.6$ is used to predict the correct spreading rate for the round jet flame [20]. To model the SGS stresses in LES a dynamic Smagorinsky model is used, as explained next.

6.3.1. MODELING TURBULENCE IN LES

Similar to the closure of Reynolds stresses in RANS, the SGS stresses in LES can be modeled based on a turbulent viscosity hypothesis:

$$R_{ij} = \bar{\rho} (\widehat{u_i u_j} - \tilde{u}_i \tilde{u}_j) = -2\mu_{SGS} \tilde{S}_{ij}^D + \frac{2}{3} \bar{\rho} k \delta_{ij}, \quad (6.32)$$

where μ_{SGS} is the SGS viscosity. k is the SGS kinetic energy defined by

$$\bar{\rho} k = \frac{1}{2} \tau_{kk} = \frac{1}{2} \bar{\rho} (\widehat{u_k u_k} - \tilde{u}_k \tilde{u}_k). \quad (6.33)$$

The SGS viscosity μ_{SGS} and SGS kinetic energy k have to be modeled. Yoshizawa's formula is often used for modeling of the SGS kinetic energy [21]:

$$\tau_{kk} = 2\bar{\rho} k = C_I 2\bar{\rho} \Delta^2 |\tilde{S}|^2, \quad (6.34)$$

where C_I is the model constant, and $|\tilde{S}| = (2\tilde{S}_{ij}\tilde{S}_{ij})^{1/2}$ is the magnitude of the strain rate tensor. Erlebacher et al [22] pointed out that for turbulent Mach numbers $M_t < 0.4$ the kinetic energy is negligible. This term can also be incorporated into a modified pressure $P = p + \frac{2}{3}k$. This leads to the a modified equation of state, which takes the form [23]:

$$P = \bar{\rho} R \tilde{v} + \frac{3\gamma - 5}{6} \tau_{kk}, \quad (6.35)$$

where $v = \tilde{T} - \frac{1}{2C_v\bar{\rho}}\tau_{kk}$ is the modified temperature, γ is the specific heat ratio. This expression shows that with typical gas properties ($\gamma = 1.4$, $c_v = 718 J/Kg \cdot K$, $\rho = 1.25 Kg/m^3$ for air at room temperature) the second term is indeed negligible , unless τ_{kk} is very large. This means that the SGS stress trace can be incorporated in the pressure with no modification to the equation of state [24], this approach is adopted in current study.

SMAGORINSKY MODEL

The Smagorinsky SGS model assumes that the kinematic SGS viscosity ν_{SGS} (m^2/s) can be described in terms of one length (Δ) and one velocity ($\Delta|\tilde{S}|$) scale. Thus, the SGS viscosity is evaluated as follows:

$$\mu_{SGS} = \bar{\rho} (C_S \Delta)^2 |\tilde{S}| = \bar{\rho} (C_S \Delta)^2 \sqrt{2\tilde{S}_{ij}\tilde{S}_{ij}}. \quad (6.36)$$

The model constant C_S is case dependent, ranging from $C_S \approx 0.1$ for strongly anisotropic turbulence [25] to $C_S \approx 0.2$ homogeneous isotropic flow [26].

DYNAMIC SMAGORINSKY MODEL

The main drawback of the Smagorinsky model is that there is no single value of model constant C_S that is universally applicable to a wide range of flows. Germano et al. [27] proposed a procedure to dynamically calculate the model constant based on an algebraic identity between the subgrid-scale stresses arising from filtering at two different filter sizes. The basic idea in this model is to apply the same SGS stress model at two different scales, and thus to adjust the constant to agree with known information form

the resolved field. A test filter G , with filter width $\hat{\Delta}$ larger than the LES filter (size $\bar{\Delta}$) is introduced.

The dynamic Smagorinsky model has been extended to compressible flow by Moin et al [28] and Martin et al [24]. The Germano identity for compressible flow has the same form as the incompressible version,

$$L_{ij} - \frac{1}{3} L_{kk} \delta_{ij} = CM_{ij}, \quad (6.37)$$

where $M_{ij} = \beta_{ij} - \hat{\alpha}_{ij}$, $\alpha_{ij} = -2\bar{\Delta}^2 \bar{\rho} |\tilde{S}_{ij}| \tilde{S}_{ij}^D$ and $\beta_{ij} = -2\hat{\Delta}^2 \hat{\rho} |\check{S}_{ij}| \check{S}_{ij}^D$, and C is the model constant. In compressible flow, the resolved turbulent stresses are $L_{ij} = (\widehat{\rho u_i \rho u_j} / \bar{\rho}) - \widehat{\rho u_i \rho u_j} / \hat{\rho}$, and the test stresses are $T_{ij} = \hat{\rho} \check{u}_i \check{u}_j - \hat{\rho} \check{u}_i \check{u}_j$ (where $\check{f} = \widehat{\rho f} / \hat{\rho}$).

Eq.(6.37) is over-determined, because it represents five independent equations for one unknown. The least squares method proposed by Lilly [29] is used here to minimize the error.

$$C = C_s^2 = \frac{\langle L_{ij}^* M_{ij} \rangle}{\langle M_{kl} M_{kl} \rangle}, \quad (6.38)$$

where $L_{ij}^* = L_{ij} - L_{kk} \delta_{ij}$. Although the angle brackets in the original formulation indicates averaging over homogeneous direction, it represents local average over computational volume [24] in the present study due to the absence of homogeneous direction in turbulent jet flames. It is well known that Eq. (6.38) may produce a negative value, which means negative SGS viscosity. This is interpreted, in some papers, as back-scattering (energy transfer from small scale eddies to large scale eddies). However, the model constant C is bounded to be non-negative in the present study, meaning $\mu_{SGS} \geq 0$. This ensures that the scalar dissipation rate of mixture fraction and progress variable variance remain non-negative, as will be discussed in Section 6.4.2.

6.4. SCALAR VARIANCES MODELING

6.4.1. MODELING VARIANCES IN RANS

The turbulent scalar dissipation rate for mixture fraction and progress variable variance $\bar{\rho} \tilde{s}_{\chi_Z}$ and $\bar{\rho} \tilde{s}_{\chi_{Y_c}}$ in Eqs. (6.29) and (6.30) can respectively be modeled as follows [26]:

$$\bar{\rho} \tilde{s}_{\chi_Z} = \bar{\rho} \tilde{\chi}_Z - \bar{\rho} \tilde{D} \left(\frac{\partial \tilde{Z}}{\partial x_j} \right)^2 = \bar{\rho} \frac{\epsilon}{k} \widetilde{Z''^2}, \quad (6.39)$$

and

$$\bar{\rho} \tilde{s}_{\chi_{Y_c}} = \bar{\rho} \tilde{\chi}_{Y_c} - \bar{\rho} \tilde{D} \left(\frac{\partial \tilde{Y}_c}{\partial x_j} \right)^2 = \bar{\rho} \frac{\epsilon}{k} \widetilde{Y_c''^2}, \quad (6.40)$$

where $\bar{\rho} \tilde{\chi}_Z$ and $\bar{\rho} \tilde{\chi}_{Y_c}$ are respectively the total scalar dissipation rate for mixture fraction and progress variable. Note that the dissipation rate in this study does not include the factor 2, different from the convention in [26]. The factor together with model constants for $\bar{\rho} \tilde{s}_{\chi_Z}$ and $\bar{\rho} \tilde{s}_{\chi_{Y_c}}$ are absorbed in the model constants $C_{d,Zv}$ and C_{d,Y_cv} , the value of which will be discussed latter. Substituting Eqs. (6.39) and (6.40) into Eqs. (6.29) and (6.30) we have the modeled transport equation for variances of mixture fraction and progress variable in URANS simulation.

6.4.2. MODELING VARIANCES IN LES

MODELING SGS SCALAR DISSIPATION RATE

The SGS part of scalar dissipation rate in Eqs. (6.29) and (6.30) can be modeled by linear relaxation models[8, 30]:

$$\bar{\rho}\tilde{s}_{\chi_Z} = \bar{\rho}\tilde{\chi}_Z - \bar{\rho}\tilde{D}\left(\frac{\partial\tilde{Z}}{\partial x_j}\right)^2 = D_t \frac{\widetilde{Z''^2}}{\Delta^2}, \quad (6.41)$$

and

$$\bar{\rho}\tilde{s}_{\chi_{Y_c}} = \bar{\rho}\tilde{\chi}_{Y_c} - \bar{\rho}\tilde{D}\left(\frac{\partial\tilde{Y}_c}{\partial x_j}\right)^2 = D_t \frac{\widetilde{Y_c''^2}}{\Delta^2}. \quad (6.42)$$

Similar to section 6.4.1, model constants for $\bar{\rho}\tilde{s}_{\chi_Z}$ and $\bar{\rho}\tilde{s}_{\chi_{Y_c}}$ are absorbed in the model constants $C_{d,Zv}$ and C_{d,Y_cv} . In [12], $\bar{\rho}\tilde{s}_{\chi_Z}$ is modeled similar to Eq. (6.41) with $C_{d,Zv} = 4$. But a distinction between conserved and non-conserved scalar was considered by linking $\bar{\rho}\tilde{s}_{\chi_{Y_c}}$ to $\bar{\rho}\tilde{s}_{\chi_Z}$ with a parameter that is evaluated using local progress variable. In the present study, dynamic procedures are proposed for determination of both $C_{d,Zv}$ and C_{d,Y_cv} as will be discussed in section 6.4.2. Substituting Eqs. (6.41) and (6.42) into Eqs. (6.29) and (6.30) we have the modeled transport equation models for SGS variances of mixture fraction and progress variable in LES simulation.

6

ALGEBRAIC MODEL

The Algebraic model can be obtained by assuming local equilibrium, namely the generation of scalar variance at SGS level is exactly balanced by its dissipation. Following this assumption, from Eqs. (6.29), (6.30), (6.41) and (6.42), the following algebraic models for mixture fraction and progress variable variance can be obtained respectively:

$$\widetilde{Z''^2} = C_{Zv}\Delta^2\left(\frac{\partial\tilde{Z}}{\partial x_i}\right)^2. \quad (6.43)$$

and

$$\widetilde{Y_c''^2} = C_{Y_cv}\Delta^2\left[\left(\frac{\partial\tilde{Y}_c}{\partial x_i}\right)^2 + \frac{Sc_t}{\mu_t}\left(\overline{Y_c\dot{w}_{Y_c}} - \tilde{Y}_c\bar{\omega}_{Y_c}\right)\right]. \quad (6.44)$$

Eq. (6.44) takes into account the influence of progress variable source term on its variance. We refer Eq. (6.43) and Eq. (6.44) as "AGM1". In many references, the influence of progress variable source term is simply neglected, resulting in the following expression:

$$\widetilde{Y_c''^2} = C_{Y_cv}\Delta^2\left(\frac{\partial\tilde{Y}_c}{\partial x_i}\right)^2. \quad (6.45)$$

We call Eq. (6.43) and Eq. (6.45) "AGM2". The model constants C_{Zv} and C_{Y_cv} for algebraic models are related to the model coefficients in transport equations by the following relations:

$$C_{Zv} = \frac{C_g}{C_{d,Zv}} \quad \text{and} \quad C_{Y_cv} = \frac{C_g}{C_{d,Y_cv}}. \quad (6.46)$$

We will discuss later the use of these relations to obtain proper model constants for the transport equation of mixture fraction and progress variable variances.

A wide range of C_{Zv} and C_{Y_cv} values from 1/12 to 0.3 have been reported in literature[11, 31–33]. Pierce and Moin [34] proposed a dynamic procedure for determination of C_{Zv} . Here we generalize this dynamic procedure to determine C_{Y_cv} for both “AGM1” and “AGM2”.

Analogous to Yoshizawa’s expression [21] for SGS kinetic energy, Eq. (6.43) can be rewritten as [34]:

$$\bar{\rho} \widetilde{Z''^2} = C_{Zv} \Delta^2 \bar{\rho} \left(\frac{\partial \tilde{Z}}{\partial x_i} \right)^2. \quad (6.47)$$

Applying a test filter with larger filter width ($\hat{\Delta} = 2\bar{\Delta}$), the Leonard term for the left-hand side is defined as:

$$L_{Zv} = [\bar{\rho} \tilde{Z} \tilde{Z}] - \hat{\bar{\rho}} \check{\tilde{Z}} \check{\tilde{Z}}, \quad (6.48)$$

where $[\]$ denotes filter at the test level, equals to $\hat{\ }^{\wedge}$.

From the right-hand side of Eq. (6.48), one obtains the model term:

$$M_{Zv} = \hat{\Delta}^2 \hat{\bar{\rho}} \left(\frac{\partial \check{\tilde{Z}}}{\partial x_i} \right)^2 - \Delta^2 [\bar{\rho} \left(\frac{\partial \tilde{Z}}{\partial x_i} \right)^2]. \quad (6.49)$$

Assuming that the model coefficient varies slowly in space and that the same coefficient applies to both filter levels, one obtains $L_{Zv} = C_{Zv} M_{Zv}$. The least-squares method proposed by Lilly [29] is also adopted here.

$$C_{Zv} = \frac{\langle L_{Zv} M_{Zv} \rangle}{\langle M_{Zv} M_{Zv} \rangle}. \quad (6.50)$$

The Leonard term for the left-hand side of Eq. (6.44) is defined as:

$$L_{Y_cv} = [\bar{\rho} \tilde{Y}_c \tilde{Y}_c] - \hat{\bar{\rho}} \check{\tilde{Y}}_c \check{\tilde{Y}}_c, \quad (6.51)$$

and the model terms for “AGM1” and “AGM2” respectively read:

$$M_{Y_cv} = \hat{\Delta}^2 \hat{\bar{\rho}} \left[\left(\frac{\partial \check{\tilde{Y}}_c}{\partial x_i} \right)^2 + \frac{Sc_t}{\hat{\mu}_t} ([\overline{Y_c \dot{\omega}_{Y_c}}] - \check{\tilde{Y}}_c \hat{\bar{\omega}}_{Y_c}) \right] - \Delta^2 [\bar{\rho} \left(\left(\frac{\partial \tilde{Y}_c}{\partial x_i} \right)^2 + \frac{Sc_t}{\mu_t} (\overline{Y_c \dot{\omega}_{Y_c}} - \tilde{Y}_c \bar{\omega}_{Y_c}) \right)], \quad (6.52)$$

and

$$M_{Y_cv} = \hat{\Delta}^2 \hat{\bar{\rho}} \left(\frac{\partial \check{\tilde{Y}}_c}{\partial x_i} \right)^2 - \Delta^2 [\bar{\rho} \left(\frac{\partial \tilde{Y}_c}{\partial x_i} \right)^2]. \quad (6.53)$$

Similar to (6.50), the least-squares method is used to obtain the model constant:

$$C_{Y_cv} = \frac{\langle L_{Y_cv} M_{Y_cv} \rangle}{\langle M_{Y_cv} M_{Y_cv} \rangle}. \quad (6.54)$$

The developed dynamic algebraic models are referred to as “Dyn-AGM1” and “Dyn-AGM2”, respectively corresponding to the calculation of M_{Y_cv} using Eq. (6.52) or (6.53).

DYNAMIC TRANSPORT EQUATION MODEL

The algebraic model assumes local equilibrium between the generation and dissipation of the scalar variances, which does not necessarily always hold [35]. The transport equation model does not have this limitation. However, on one hand, optimal value for the model constants $C_{d,Zv}$ and $C_{d,Ycv}$ in the transport equation for the variances of mixture fraction and progress variable are not available a priori to the simulation. On the other hand, as will be discussed in section 6.6.2, the flame lift-off height is very sensitive to these model constants. Kual et al [35] showed that these constants vary significantly depending on local condition and filter size, and they proposed a dynamic procedure to determine the model coefficients for the transport equation of mixture fraction variance. From the simulation with this dynamic transport equation, the $D_{d,Zv}$ was found in the range between 2 to 13 in the reaction region. However, this model requires time derivative of the variance Leonard term and is difficult to extend to the transport equation of $\widetilde{Y_c''^2}$.

In this study, we propose to use relations (6.46) to dynamically obtain the model constant for the transport equations of $\widetilde{Z''^2}$ and $\widetilde{Y_c''^2}$. As explained in section 6.4.2, C_{Zv} and C_{Ycv} are obtained under equilibrium assumption, they lead to over-dissipation of SGS variances. To consider the non-equilibrium effect, two new constants $\gamma_{eq,Z}$ and $\gamma_{eq,Yc}$ are introduced in the relations between the algebraic and transport equation model constants. The new relations read:

$$C_{d,Zv} = \gamma_{eq,Z} \frac{C_g}{C_{Zv}} \quad \text{and} \quad C_{d,Ycv} = \gamma_{eq,Yc} \frac{C_g}{C_{Ycv}} \quad (6.55)$$

The physical meaning of $\gamma_{eq,Z}$ and $\gamma_{eq,Yc}$ can be interpreted as extent of local equilibrium that has been achieved, therefore they are referred to as equilibrium constants. They should be in the range of $[0,1]$, $\gamma_{eq,Z} = 1$ and $\gamma_{eq,Yc} = 1$ meaning a fully equilibrium condition. From simulations adopting dynamic algebraic models, C_{Zv} , C_{Ycv} are found predominantly to have values smaller than 0.1, which means $C_{d,Zv}$ and $C_{d,Ycv}$ greater than 20 if $\gamma_{eq,Z} = \gamma_{eq,Yc} = 1$. These values are much larger than the commonly used values for the transport equations models (around 2), which suggests that the non-equilibrium effect maybe significant. Therefore a small value of $\gamma_{eq,Z}$ and $\gamma_{eq,Yc}$ is reasonable, in this case $\gamma_{eq,Z} = \gamma_{eq,Yc} = 0.35$ are used. A further study is needed in future to pursue a dynamic method to determine these equilibrium constants.

The procedure of solving the dynamic transport equation model is summarized as following:

Step1: the dynamic algebraic model Eqs. (6.50) and (6.54) are solved. Algebraic model constants, C_{Zv} and C_{Ycv} are obtained according to local conditions.

Step2: model constants for the transport equation models, $C_{d,Zv}$ and $C_{d,Ycv}$, are deduced via (6.55).

Step3: finally the transport equations (6.29) and (6.30) with the dynamically determined model constants are solved.

Since the dynamic transport equation can be formed by coupling either “AGM1” or “AGM2” with the transport equation model, the following two dynamic transport equation models should be distinguished: “DynTP-AGM1” and “DynTP-AGM2”.

6.5. NUMERICAL METHODOLOGY

6.5.1. FGMFOAM SOLVER

The simulation in this study is carried out with the open source CFD package – OpenFOAM [14]. New libraries have been created for the FGM storage and retrieval algorithms and are dynamically linked to a customized solver. The new solver is referred to as “FGMFoam”. FGMFoam is based on the PIMPLE algorithm, a combination of PISO (Pressure implicit with splitting of operator) [36] and SIMPLE (Semi-Implicit Method for Pressure-Linked Equations) [25] algorithms. The algorithm of this solver is shown in Fig 6.2. Transport equations for the controlling variables are solved after the velocity prediction step. Then necessary properties, e.g. \tilde{T} , $\tilde{\mu}$ and $\tilde{\omega}_{Y_c}$, are retrieved from the FGM libraries with the newly obtained controlling variables. Note that between the solution of the controlling parameter and the FGM lookup, there is a necessary step to convert the solved controlling parameters (\tilde{Z} , $\tilde{Z''^2}$, \tilde{Y}_c , $\tilde{Y''^2}$) to the controlling parameters used to construct the FGM libraries (\bar{Z} , $\bar{\zeta}_Z$, \bar{C} , $\bar{\zeta}_C$). The relations between these controlling parameters are given in Table 6.2. After this, the velocity-pressure correction is conducted within the PISO loop. One PIMPLE loop and three PISO loops are carried for each time step in both URANS and LES simulation.

6.5.2. NUMERICAL DETAILS

For the URANS simulation, a 2D axisymmetric configuration was adopted. Mean velocity of fuel and coflow streams from experiment are specified as boundary conditions. For the LES, a 3D cylindrical geometry with radius of 22D and length of 100D is used, where D is the diameter of the fuel nozzle. The turbulent inlet boundary condition is provided by a separate pipe simulation using periodic boundary condition. The axial direction is discretized with 495 grid points, radial direction is discretized with 96 grid points and the circumferential direction is equally divided by 72 points, resulting in a total mesh size of 3.2 million. The smallest filter size is 0.12 mm ($\approx 0.03D$) at the centerline near the fuel jet exit, and the largest filter size is 5 mm ($\approx 1.09D$) at the largest radial distance on the exit plane. Two cross sections of the 3D mesh used in the LES cases are shown in Fig. 6.3.

The transport equations are spatially discretized with a Finite Volume Method (FVM). The convection and Laplacian terms are discretized respectively by second-order accuracy total variation diminishing (TVD) schemes ‘Gauss van Leer’ and ‘Gauss van Leer corrected’. Implicit second-order method CrankNicholson with blending factor $\phi = 1.0$ is used for the temporal integration. For the URANS simulation, an adjustable time step with maximum Courant number 0.5 is used to specify the simulation time step. In the LES cases, the time step is fixed as 5×10^{-7} s. The steady state is reached at around 0.03 s from the initial state. Averaging of properties starts at 0.05 s, corresponding to roughly 10 flow-through time based on the fuel jet mean velocity. Averaging duration is 0.1 s. The LES is carried out on the Cartesius supercomputer [37]; around 5000 CPU hours is required for one case.

6.6. RESULTS AND DISCUSSION

The results will be presented in three parts. The ignition process and flame structure of the studied flame is analyzed in the first part. In this part we show that the flame studied

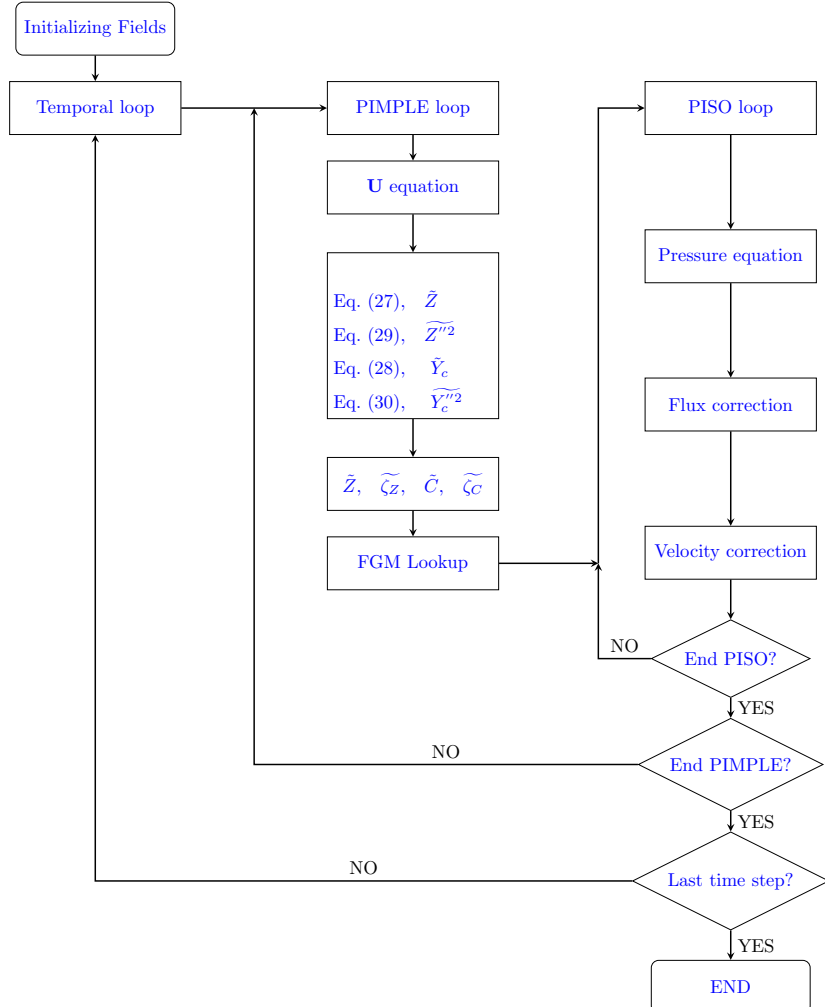


Figure 6.2: Algorithm of the FGMFoam slover

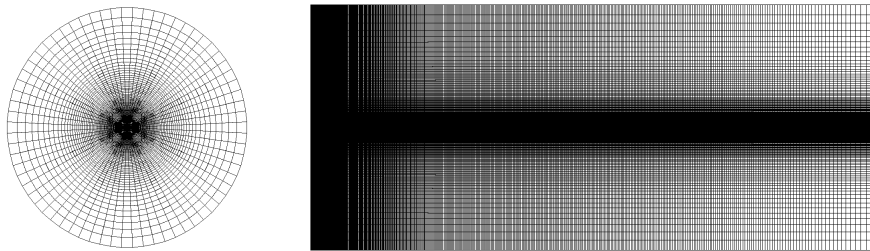


Figure 6.3: Two cross-sections of the 3D mesh for the LES case.

is mainly stabilized by auto-ignition. Based on this knowledge, the sensitivity of the auto-ignition process on the model constants in the transport equations of mixture fraction and progress variable variances are analyzed. In the last part, results obtained with the proposed new dynamic models for determining these model constants are shown and performance of different models are compared.

6

6.6.1. IGNITION PROCESS AND FLAME STRUCTURE

Fig. 6.4 shows a snapshot of instantaneous flow field. In this figure, the iso-surface of stoichiometric mixture fraction is used to show the mixing between fuel and oxidizer streams, the iso-surface of $T = 1800\text{K}$ is plotted to represent the reaction region and the streamlines provide information on the flow pattern. The mixing of the central jet with high-temperature coflow before the flame base is clearly visible from this figure. The flame stabilized at approximately 40 times the fuel jet diameter downstream the fuel exit. The temperature fields on a cross section with iso-line of $T = 1800\text{K}$ at four sequential time steps are depicted in Fig. 6.5. At time t_0 , a few hot spots are firstly formed at the lean side of the jet. These ignited spots gradually increase as they are convected downstream and merge together at the flame base from time $t_0 + dt$ to $t_0 + 3dt$. As experimentally revealed by Oldenhoef et al. [38] the occurrence and growth of the ignition kernels provide strong evidence for the auto-ignition mechanism of flame stabilization. Furthermore, the accumulation of HO_2 before the flame base as shown in Fig. 6.6 is another sign of auto-ignition. Comparing the contour plot of HO_2 and OH , the rich HO_2 regions are located right before the region where the high value of OH starts. Mir Najafizadeh et al [39] studied the chemical structure of a H_2/N_2 flame under similar coflow condition as the flame studied in this paper, they found that the auto-ignition has a large contribution to the stabilization of that flame and near the flame base the OH is formed by consuming HO_2 at a very lean condition. Based on these observations, it can be confirmed that the auto-ignition is indeed the main stabilization mechanism for this flame.

To further investigate the flame structure, two flame indices are defined respectively based on the reactions between CH_4 with O_2 and CO with O_2 .

$$FI_{\text{CH}_4} = \nabla Y_{\text{CH}_4} \cdot \nabla Y_{\text{O}_2}, \quad (6.56)$$

and

$$FI_{CO} = \nabla Y_{CO} \cdot \nabla Y_{O_2}. \quad (6.57)$$

Snapshots of these two flame indices are given in Fig. 6.6. The FI_{CH_4} predominantly show positive values, especially before the flame base. This however, does not mean that the CH_4 is consumed in a premixed combustion mode in this region. The alignment of the CH_4 and O_2 gradients in this region is mainly caused by the fact that in this flame the central jet is already a premixed mixture with even higher content of O_2 than the coflow. The mixing with coflow as the jet develops actually dilutes both CH_4 and O_2 , resulting in a positive value of FI_{CH_4} at the shear layer. The heat release region indicated by the overlapping of OH and CH_2O ($Y_{OH} \times Y_{CH_2O}$) is also displayed in Fig. 6.6. Both negative and positive values of FI_{CH_4} are observed on the flame front. This reveals that the CH_4 reacts with O_2 in both premixed and non-premixed combustion modes. The flame index FI_{CO} shows rather interesting results in the sense that the regions with negative values of FI_{CO} corresponds well with the heat release region, meaning that the reaction of CO is substantially responsible for heat release and it happens predominantly in a non-premixed mode. This is quite reasonable, since the CO and H_2 are formed by fuel rich combustion, and can only be consumed by O_2 from coflow in the shear layer. Moreover, from the results of heat release region and flame indices, it is found that the reaction is mostly happening on a thin and distorted flamelet structure, justifying the applicability of FGM in the simulation of this flame.

6

The above analysis showed that this flame is mainly stabilized by the formation and growth of ignition kernels. Both premixed and non-premixed combustion modes are detected. As the β -function PDF is used for both mixture fraction and progress variable in the current study, the variances of these two scalars influence the local properties that are retrieved from the FGM table and consequently influence the auto-ignition process. The sensitivity of the results on the scalar variance model constants will be investigated using URANS results in the next section.

6.6.2. SENSITIVITY OF FLAME LIFT-OFF ON MODEL CONSTANTS

Results of a parameter study in order to explore the sensitivity of auto-ignition process on the mixture fraction and progress variable variances model constants are shown in this section. The value of model constants $C_{d,Zv}$ and $C_{d,Ycv}$ in the transport equation of mixture fraction and progress variable variances are varied around their commonly used values 2. A temperature contour plot is shown in Fig. 6.7 supplemented with an isoline of OH mass fraction equal to 0.0005. The flame lift-off height is defined in this study as the lowest axial location where the $Y_{OH} = 0.0005$ is reached. Fig. 6.7 shows a significant sensitivity of the flame lift-off height on the model constants $C_{d,Zv}$ and $C_{d,Ycv}$. Since $C_{d,Zv}$ and $C_{d,Ycv}$ are the model constants for the dissipation terms in the transport equations of mixture fraction and progress variable variance, lower value of these two constants mean less dissipation, thus higher fluctuation. The flame lift-off height is influenced by these two parameters in a complicated manner. At relatively high fluctuation of mixture fraction ($C_{d,Zv} = 1$), the flame always ignites despite the change of progress variable fluctuation ($C_{d,Ycv} = 1, 2$ and 3). However, the lift-off height of the flame decreases with decrease of progress variable variance (increasing of $C_{d,Ycv}$). At relatively low fluctuation of mixture fraction ($C_{d,Zv} = 3$), the flame does not ignite when the fluctuation of

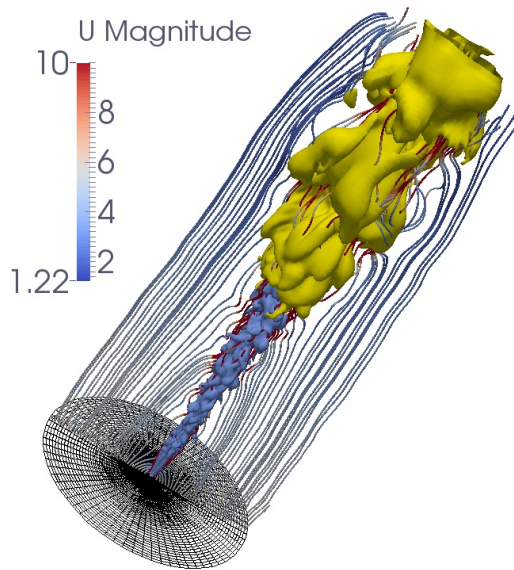


Figure 6.4: Flame configuration, iso-surface of stoichiometric mixture fraction ($Z = 1.77$, blue), iso-surface of $T = 1800$ K (yellow) and streamlines colored by flow velocity.

6

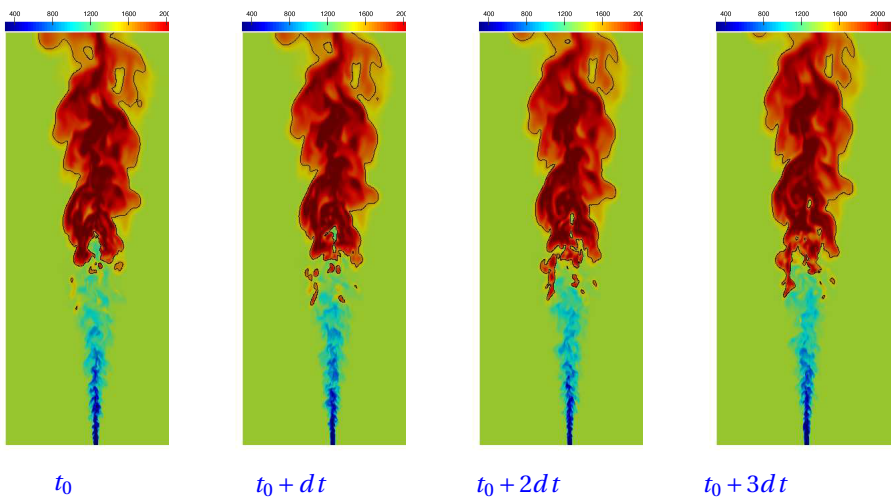


Figure 6.5: Snapshots of temperature contour plot.

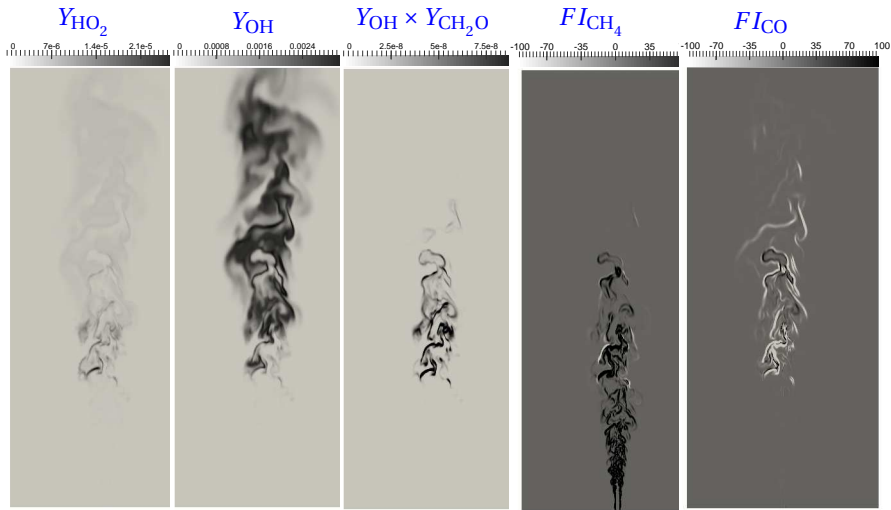
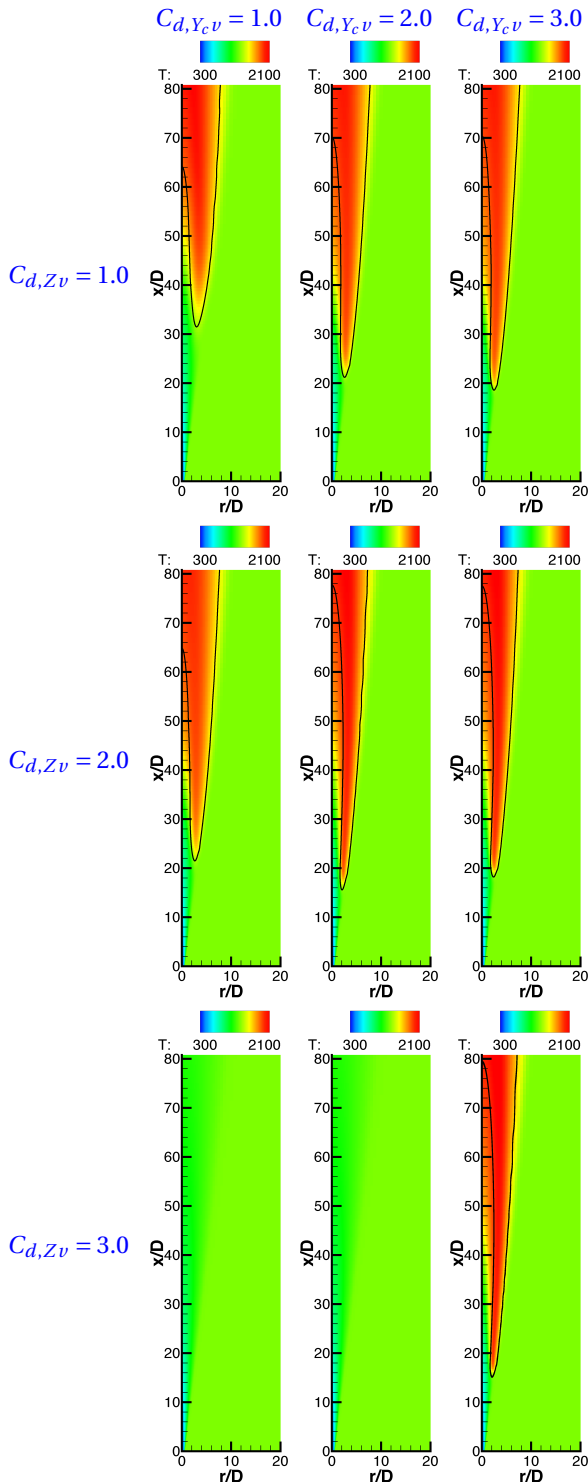


Figure 6.6: Snapshot of species mass fraction and flame index from LES simulation.

6

progress variable is high ($C_{d,Y_c}v = 1$ and 2). When the fluctuation of progress variable is further suppressed ($C_{d,Y_c}v = 3$), the flame ignites and the lowest lift-off height among all the cases is observed. Fixing the value of $C_{d,Y_c}v$ (column-wise comparison), the flame lift-off height first decreases with the increase of $C_{d,Zv}$, but further increase of $C_{d,Zv}$ may lead to no ignition, depending on the level of mixture fraction fluctuation. Given low level of mixture fraction fluctuation ($C_{d,Zv} = 3$), the flame lift-off height is extremely sensitive to the change of $C_{d,Y_c}v$ within a certain range. A finer parameter study on this is shown in Fig. 6.8. An over- or under-prediction of the flame lift-off height is experienced by varying $C_{d,Y_c}v$ from 2 to 3.

Radial profiles of the mean temperature from three representative cases are shown in Fig. 6.9. The sensitivity of the results on the model constants is evident when compared to experimental data. This sensitivity has two causes: on one hand, as investigated by Domingo et al [30] the ignition delay time of this flame reaches its minimum at the very lean side ($Z \approx 0.00427$) and rapidly increases away from this condition. This means that a small variation on the mixing at the lean side would lead to a large change in the ignition delay and therefore the flame lift-off height. On the other hand, the sensitivity is an essential feature of RANS simulation, where all the effects of turbulent fluctuations are modeled. These turbulence and scalar variance models rely on many empirical constants. Studies have shown that these model constants widely vary from case to case, and no optimal value is available in priori to the simulation of a new case. Therefore a wide range of these constants have been reported in the literature, even for simulation of similar or same experimental cases. By fine-tuning the model constants, a very good agreement on the mean properties can be achieved between simulation results and experimental data in the URANS, as shown by the case with $C_g = 2.86$ and $C_{d,Zv} = C_{d,Y_c}v = 1.0$ in Fig. 6.9. However, the general goal of the numerical combustion modeling research is to develop a predictable, robust and widely applicable tool for practical applications.



6

Figure 6.7: Contour plot of temperature with isoline of $Y_{OH} = 0.0005$ ($C_g = 2$), URANS.

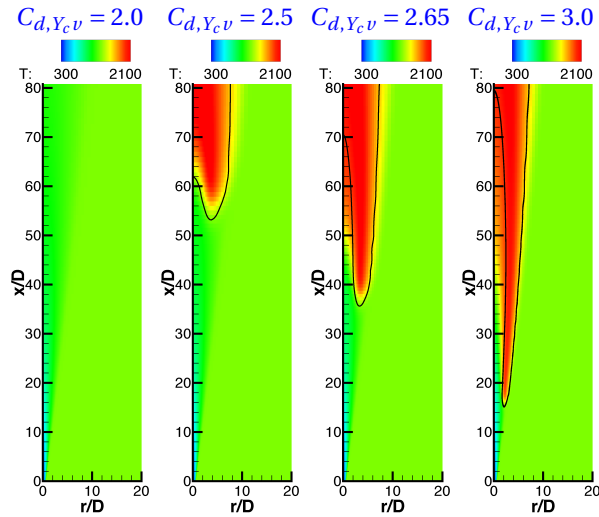


Figure 6.8: Contour plot of temperature with isoline of $Y_{OH} = 0.0005$ ($C_g = 2.0$, $C_{d,Zv} = 3.0$), URANS.

6

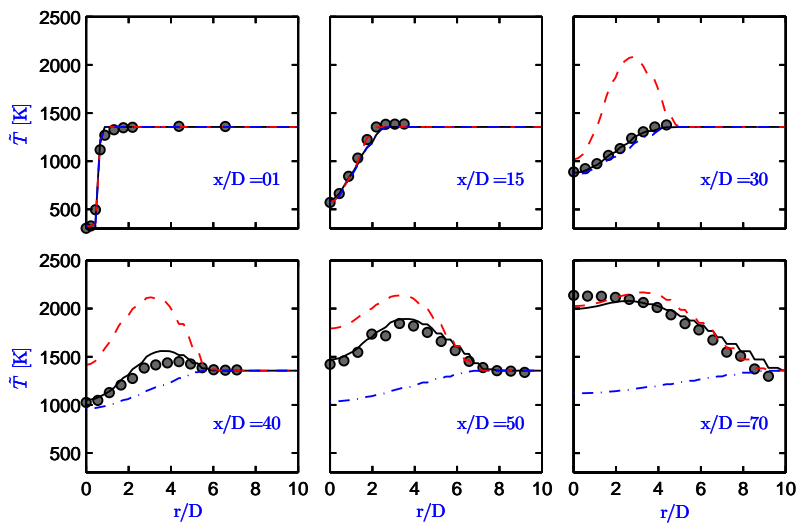


Figure 6.9: Radial profiles of mean temperature from URANS, $C_g = 2.86, C_{d,Zv} = 1, C_{d,Y_cv} = 1$ (—), $C_g = 2, C_{d,Zv} = 2, C_{d,Y_cv} = 1$ (- - -), $C_g = 2, C_{d,Zv} = 3, C_{d,Y_cv} = 1$ (- · -), Experiment (●).

Based on this criteria, it is clear that the tuning of model constants within RANS simulation for this kind of auto-ignition flame is ad-hoc and therefore less valuable.

6.6.3. RESULTS OF DYNAMIC SGS VARIANCE MODELS

LES provides possibilities to dynamically determine the uncertain model constants. In this section, results from LES simulation using dynamic Smagorinsky model and dynamic scalar variances model as proposed in Section 6.4 will be analyzed. Four cases that will be analyzed are summarized in Table. 6.3.

Table 6.3: LES cases description.

Case name	SGS variance model	coefficients
Ag1	DynAGM1	/
Ag2	DynAGM2	/
Tp1	DynTP-AGM1	$\gamma_{eq,Z} = \gamma_{eq,Y_c} = 1.0$
Tp2	DynTP-AGM1	$\gamma_{eq,Z} = \gamma_{eq,Y_c} = 0.35$

INFLUENCE OF FLUCTUATING SOURCE TERM ON $\widehat{Y_c''^2}$

As shown by Eq. (6.44), the fluctuation of the progress variable source term also contributes to its variance. This term is however, most often neglected, for example in the commercial software ANSYS Fluent [40]. The importance of this term is investigated in the present section by comparing results from cases respectively using “Dyn-AGM1” and “Dyn-AGM2”. The influence of fluctuating source term on progress variable variance is neglected in the latter model (see Eq.(6.45)).

Comparison between case “Ag1” and “Ag2” showed that the fluctuation of the progress variable source term indeed has a non-negligible effect when the algebraic model is used. In Fig. 6.10 and 6.11, in which the variances of mixture fraction and progress variables are shown, one can see that, as expected, case “Ag2” in general predicts smaller variances than case “Ag1”, since the generation of $\widehat{Y_c''^2}$ due to fluctuation of Y_c source term is neglected in case “Ag2”. It is worth mentioning that the experimental data for progress variable variances plotted here are actually not accurate. Indeed, because based on the definition of the progress variable used in this study (Eq. (6.5)), the value of $\widehat{Y_c''^2}$ requires the information on the covariances of the mass fraction of the involved species (CO_2 , H_2O , CO and H_2). However, this information is not available in the experimental dataset. The plotted experimental $\widehat{Y_c''^2}$ is simply the sum of the measured variances of each species. This value is plotted here only as a reference. If the mean temperature (Fig. 6.12) and mean species mass fraction (Fig. 6.13) are considered, results of case “Ag2” even have better agreement with the experimental data compared to those of case “Ag1”. Similar to the observations made in section 6.6.2, again we found that the influence of the variances of FGM controlling parameters on the auto-ignition process is not really straightforward. This is of course due to the strong TCI, all the variables and processes are strongly coupled. Improvement on only one aspect of the entire model system does not necessarily lead to a better prediction of the whole system. So under the equilibrium

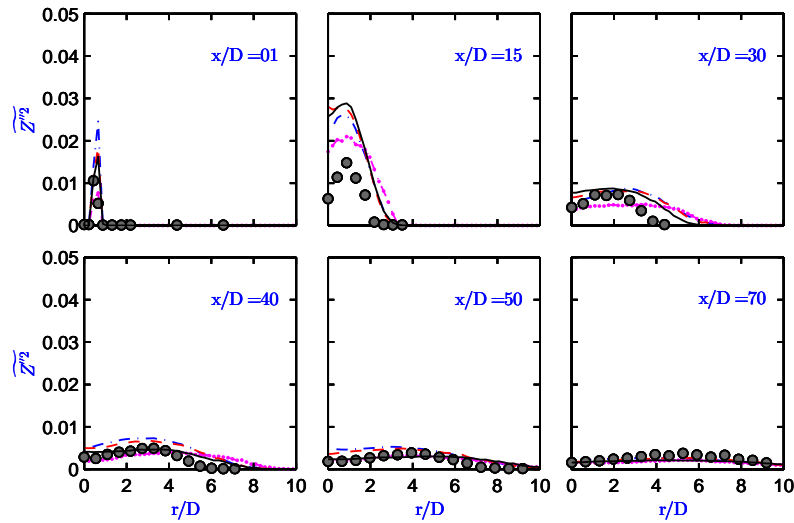


Figure 6.10: Radial profiles of mean mixture fraction variance, results of LES, Ag1: (— · —), Ag2:(— ● —), Tp1 (— - -), Tp2 (— —), Experiment (●).

6

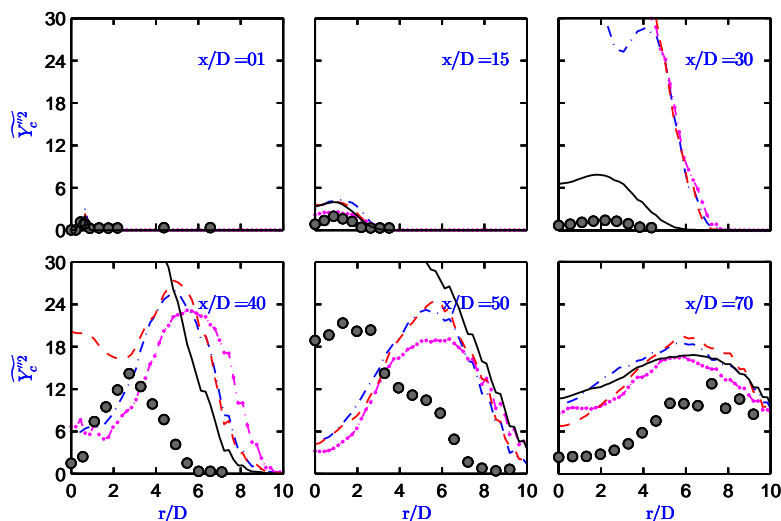


Figure 6.11: Radial profiles of mean progress variable variance, results of LES, Ag1: (— · —), Ag2:(— ● —), Tp1 (— - -), Tp2 (— —), Experiment (●).

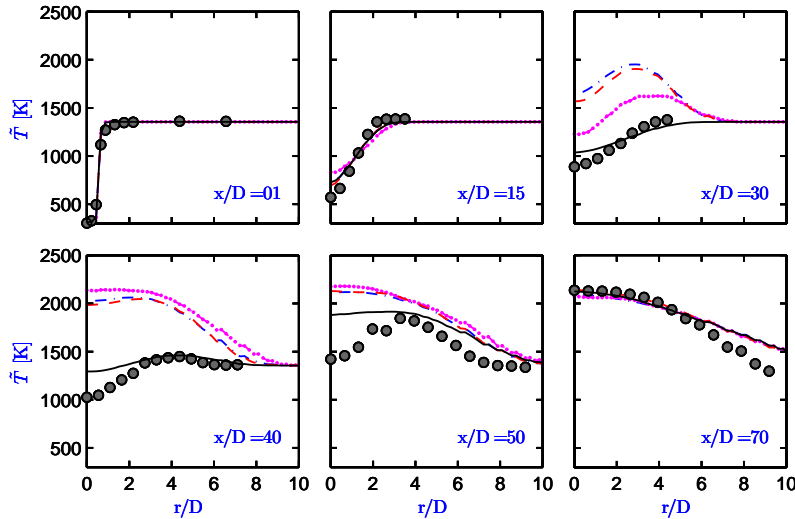


Figure 6.12: Radial profiles of mean temperature, results of LES, Ag1: (— · —), Ag2:(— ● —), Tp1 (— - -), Tp2 (— — —), Experiment (●).

assumption, it is difficult to fairly assess the effect of the inclusion of the extra source term in the $\widetilde{Y_c''^2}$ model on the whole system. This also suggests that simulations using models “AGM2” or “Dyn-AGM2” may have success by luck, because the underestimation of the progress variable variances due to the equilibrium assumption may be compensated by the effect of exclusion of the fluctuating source term. Simulations respectively using dynamic transport equation models “DynTP-AGM1” and “DynTP-AGM2” were also carried out (not shown here for simplicity), the results showed that using “DynTP-AGM1” indeed slightly improved the prediction.

ALGEBRAIC MODE VS. TRANSPORT EQUATION MODEL

The performances of the dynamic algebraic model “DynAGM1” and dynamic transport equation model “DynTP-AGM1” are analyzed in this subsection. Compared to experimental data, case “Ag1” significantly over-predicts the mean temperature (Fig. 6.12), and mean progress variable (Fig. 6.14) between axial stations $x/D = 30$ to 50 . The progress variable variance $\widetilde{Y_c''^2}$ (Fig. 6.11) was predicted much higher in case “Ag1” than the plotted experimental data and those of the case “Tp2” at $X/D = 30$, and the opposite was observed at $X/D = 40$ and $X/D = 50$. Similar results can also be seen in the root mean square (RMS) value of the mass fraction of main combustion products, i.e. CO_2 and H_2O , in Fig. 6.15. Meanwhile, over-prediction of these combustion products from $x/D = 30$ is also evident in case “Ag1”, see Fig. 6.13. Based on these results, we can conclude that the flame stabilizes at around $X/D = 30$ in case “Ag1”, which is lower than reported by experimental study [13] and a previous simulation [12]. This is because the ignition takes place too early and the flame lift-off height is under-predicted. In this case, the dynamic algebraic model “Dyn-AGM1” (Eq. (6.44)) was used for the determination of the mixture

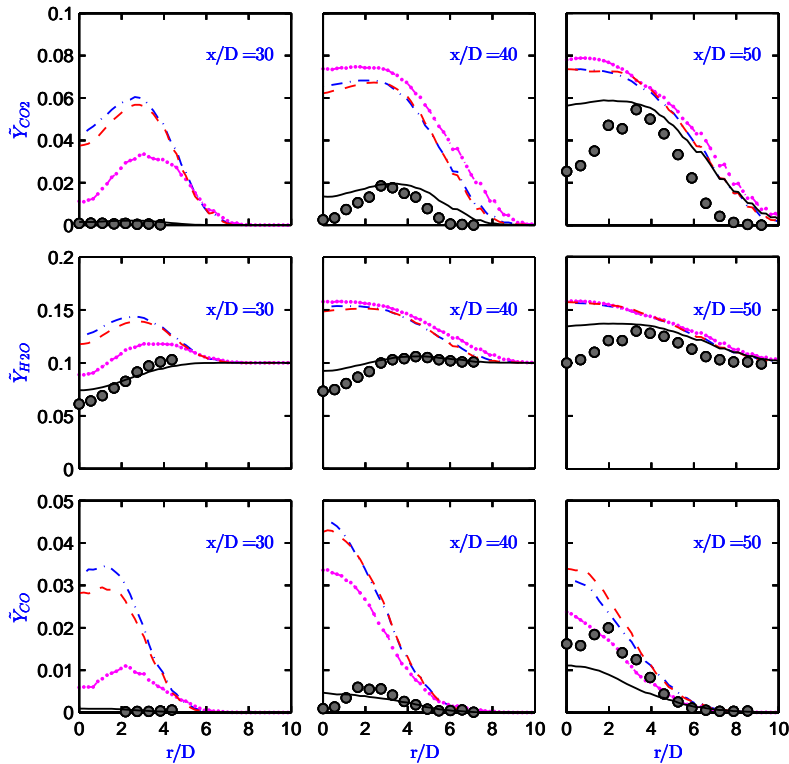


Figure 6.13: Radial profiles of mean species mass fraction, results of LES, Ag1: (— · —), Ag2:(— ● —), Tp1 (— - -), Tp2 (—), Experiment (●).

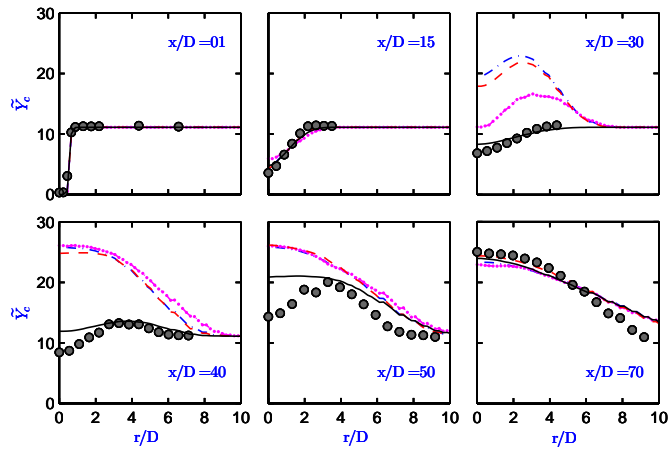


Figure 6.14: Radial profiles of mean progress variable, results of LES, Ag1: (— · —), Ag2:(— ● —), Tp1 (— - -), Tp2 (—), Experiment (●).

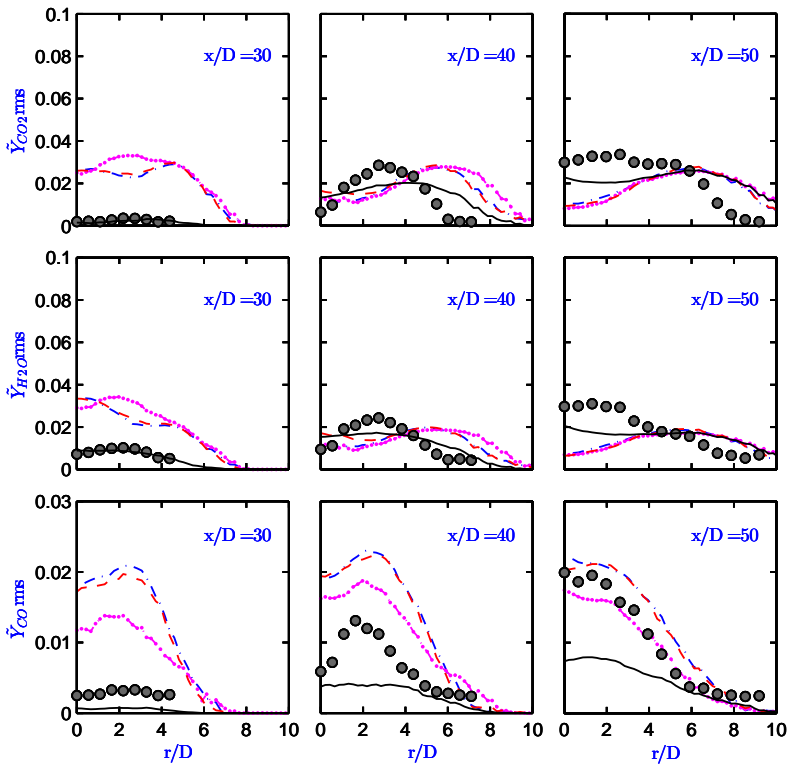


Figure 6.15: Radial profiles of species mass fraction root mean square (RMS), results of LES, Ag1: (\cdots), Ag2:(\cdots), Tp1 (\cdots), Tp2 (—), Experiment (●).

fraction and progress variable variances. Unsurprisingly, in case “Tp1”, in which the dynamic transport equation model “DynTP-AGM1” with $\gamma_{eq,Z} = \gamma_{eq,Y_c} = 1.0$ is employed, only slight improvements have been achieved. This is because, in case “Tp1”, the dissipation term coefficients for the transport equations of \widetilde{Z}'' and $\widetilde{Y_c}''^2$ are directly converted from the dynamic algebraic model “Dyn-AGM1” using relations (6.46). In the algebraic model, the local equilibrium assumption was made. This assumption leads to an over-dissipation of the scalar variances in both “Ag1” and “Tp1” cases. The over-dissipation of the scalar variances, especially $\widetilde{Y_c}''^2$, tends to extend the sub-grid scale ignition event, which cannot be computationally resolved, and this in turn leads of under-prediction of flame lift-off height [12].

NON-EQUILIBRIUM EFFECT

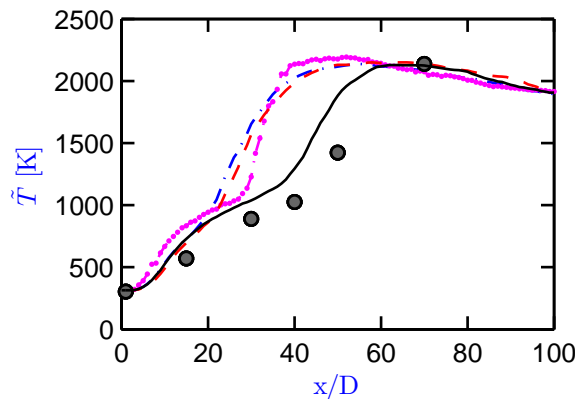


Figure 6.16: Centerline profiles of mean temperature, results of LES, Ag1: (— · —), Ag2:(— ● —), Tp1 (— - -), Tp2 (— —), Experiment (●).

When the non-equilibrium effect was considered by setting the coefficients $\gamma_{eq,Z} = \gamma_{eq,Y_c} = 0.35$, results were obtained with a considerable closer agreement with the experimental data in case “Tp2”. The radial and centerline profiles of mean temperature (Figs. 6.12 and 6.16) indicate that a significant temperature rise occurred in regions between $x/D = 40$ and $x/D = 50$. This is in agreement with the conclusion drawn in a previous LES study of this flame using an unsteady flamelet/progress variable model [12]. However, the mean temperature in the near centerline region from $x/D = 15$ downstream was under-predicted. The mean mixture fraction is under predicted in the same region, as can be seen in Fig. 6.17. These observations all point to the fact that the fuel jet breakup happened in a shorter distance from the nozzle tip in the simulation as it should be. Consequently, a leaner condition which is favorable for ignition to take place was formed in the center. Ignition kernels may appear in this region, resulting in a over-prediction on the mean temperature. The early fuel jet breakup may relate to the specification of the inlet boundary condition, as argued by Müller et al in [41]. The mean mass fraction of CO_2 , H_2O and their root mean square (RMS) values were well captured in case “Tp2”, as shown in Figs. 6.13 and 6.15. However CO was under-predicted, this may relate

to the definition of the progress variable used in this study (Eq. (6.5)), in which the contribution of CO is suppressed by using a relatively small weighting factor to maintain the monotonicity. To improve this, an optimization of the definition of progress variable is needed.

Summarizing the discussions in this section. We found that the fluctuating source term of progress variable has a considerable influence on the predicted results, however the inclusion of this term in the algebraic model does not necessarily lead to an improved prediction. This is due to the strong coupling between models. Furthermore, the equilibrium assumption made in the algebraic model has shown to be a poor assumption. The superior performance of the dynamic transport equation model with low value of equilibrium constant was demonstrated. This model is therefore recommended to be used with FGM for cases in which strong TCI exists.

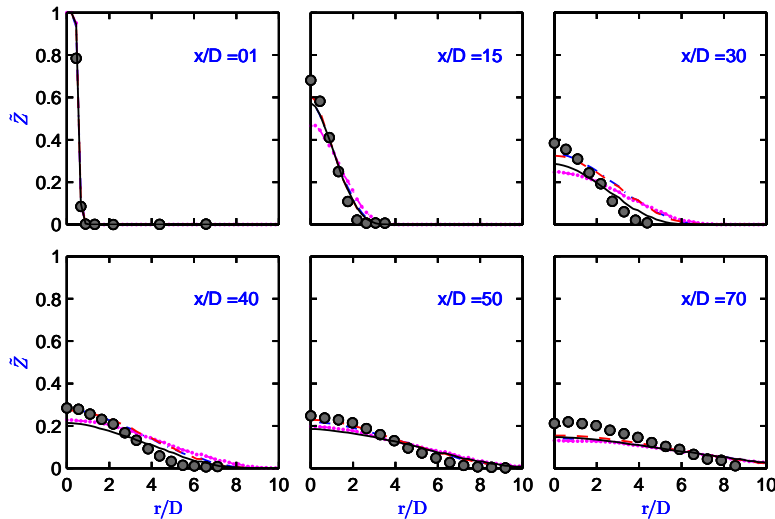


Figure 6.17: Radial profiles of mean mixture fraction, results of LES, Ag1: (---), Ag2:(-●-), Tp1 (- - -), Tp2 (—), Experiment (○).

6.7. CONCLUSIONS

In this Chapter we reported a new development in the modeling of sub-grid variances of the controlling parameters of the FGM model. In cases where the turbulence-chemistry interaction (TCI) is important, for example the auto-ignition process, the evaluation of the variances greatly influences the PDF of the controlling parameters, and therefore affects the prediction of TCI. The existing models for the scalar variances contain some empirical model constants of which no optimal value exists for wide range of applications. In this paper we have shown that in an URANS simulation, the auto-ignition process is very sensitive to even a small variation of these model constants. This brings in a considerable uncertainty when a new case is to be simulated with this model and no a priori information on these model constants is available. Therefore, the RANS technique

is not recommended for simulating cases in which strong TCI exists.

To overcome the uncertainties on the model constants choice, a dynamic procedure has been developed in the context of LES. In this model approach, the SGS Reynolds stresses are closed with the dynamic Smagorinsky model. The unknown model constants in the algebraic model and transport equation model for the controlling variable variances are calculated according to local conditions on the fly. The dynamic constants for the transport equation model are deduced from those of the dynamic algebraic model. The latter one builds on the local equilibrium assumption which was shown in this study to be a poor assumption. The non-equilibrium effect was considered by introducing a constant during the conversion of algebraic model constant to those of the transport model. The physical meaning of this constant can be interpreted as the extent of equilibrium that is achieved locally. A significant improvement on the prediction of the considered case was achieved with the dynamic transport equation model using a low value of equilibrium constants. The influence of the fluctuating source term on the variance of progress variable is also considered in the proposed dynamic SGS variance model, which has been shown to have a non-negligible influence on the prediction when algebraic model is used. The promising performance of the developed dynamic transport equation model was demonstrated.

6

APPENDIX: DERIVATION OF VARIANCE TRANSPORT EQUATIONS FOR Z AND Y_c

The derivation process for the transport equations of mixture fraction and progress variable variances will be given in this appendix. The continuity equation and exact transport equations for mixture fraction and progress variable are first given:

$$\frac{\partial \rho}{\partial t} + \frac{\partial \rho u_j}{\partial x_j} = 0 \quad (6.58)$$

$$\frac{\partial \rho Z}{\partial t} + \frac{\partial \rho u_j Z}{\partial x_j} = \frac{\partial}{\partial x_j} \left(\rho D \frac{\partial Z}{\partial x_j} \right) \quad (6.59)$$

$$\frac{\partial \rho Y_c}{\partial t} + \frac{\partial \rho u_j Y_c}{\partial x_j} = \frac{\partial}{\partial x_j} \left(\rho D \frac{\partial Y_c}{\partial x_j} \right) + \dot{\omega}_{Y_c} \quad (6.60)$$

where $\dot{\omega}_{Y_c}$ is the source term for progress variable due to reaction.

Applying Reynolds averaging or filter function to Eqs. (6.59) and (6.60), one obtains:

$$\frac{\partial \bar{\rho} \tilde{Z}}{\partial t} + \frac{\partial \bar{\rho} \tilde{u}_j \tilde{Z}}{\partial x_j} = \frac{\partial}{\partial x_j} \left(\bar{\rho} D \frac{\partial \tilde{Z}}{\partial x_j} - \Phi_{Z,j} \right) \quad (6.61)$$

$$\frac{\partial \bar{\rho} \tilde{Y}_c}{\partial t} + \frac{\partial \bar{\rho} \tilde{u}_j \tilde{Y}_c}{\partial x_j} = \frac{\partial}{\partial x_j} \left(\bar{\rho} D \frac{\partial \tilde{Y}_c}{\partial x_j} - \Phi_{Y_c,j} \right) + \bar{\omega}_{Y_c} \quad (6.62)$$

where Φ_Z and Φ_{Y_c} are respectively the (SGS) turbulent fluxes for mixture fraction and progress variable and are shown in Table 6.1.

The variance of progress variable can be obtained by:

$$Y_{c,v} = \widetilde{Y_c''^2} = \widetilde{Y_c^2} - \widetilde{Y_c}^2 \quad (6.63)$$

The transport equation for Y_c^2 can be derived by multiplying Eq. (6.60) with $2Y_c$ and making use of continuity equation Eq. (6.58):

$$\frac{\partial \rho Y_c^2}{\partial t} + \frac{\partial \rho u_j Y_c^2}{\partial x_j} = \frac{\partial}{\partial x_j} \left(\rho D \frac{\partial Y_c^2}{\partial x_j} \right) - \rho \chi_{Y_c} + 2Y_c \dot{\omega}_{Y_c} \quad (6.64)$$

where the scalar dissipation rate for Y_c is $\chi_{Y_c} = D \left(\frac{\partial Y_c}{\partial x_j} \right)^2$, D being the diffusivity.

Applying Reynolds averaging or filter function to Eq. (6.64):

$$\frac{\partial \bar{\rho} \widetilde{Y_c^2}}{\partial t} + \frac{\partial \bar{\rho} \bar{u}_j \widetilde{Y_c^2}}{\partial x_j} = \frac{\partial}{\partial x_j} \left(\bar{\rho} D \frac{\partial \widetilde{Y_c^2}}{\partial x_j} - \Phi_{Y_c^2,j} \right) - 2\bar{\rho} \tilde{\chi}_Z + \overline{2Y_c \dot{\omega}_{Y_c}} \quad (6.65)$$

where $\Phi_{Y_c^2,j} = \left(\overline{\rho u_j Y_c^2} - \bar{\rho} \widetilde{u_j} \widetilde{Y_c^2} \right)$ which for RANS can be written as $\Phi_{Y_c^2,j} = \bar{\rho} \widetilde{u_j''} \left(\widetilde{Y_c^2} \right)''$.

Similarly, the transport equation for $\widetilde{Y_c}^2$ can be derived by $2\widetilde{Y_c} \times$ Eq. (6.62) and a bit manipulation:

$$\frac{\partial \bar{\rho} \widetilde{Y_c}^2}{\partial t} + \frac{\partial \bar{\rho} \bar{u}_j \widetilde{Y_c}^2}{\partial x_j} = \frac{\partial}{\partial x_j} \left(\bar{\rho} D \frac{\partial \widetilde{Y_c}^2}{\partial x_j} \right) - 2\bar{\rho} D \left(\frac{\partial \widetilde{Y_c}}{\partial x_j} \right)^2 - \frac{\partial}{\partial x_j} (2\widetilde{Y_c} \Phi_{Y_c,j}) + 2\Phi_{Y_c,j} \frac{\partial \widetilde{Y_c}}{\partial x_j} + 2\widetilde{Y_c} \bar{\omega}_{Y_c} \quad (6.66)$$

Subtracting Eq. (6.66) from Eq. (6.65), we finally obtain the transport equation for progress variable variance:

$$\begin{aligned} \frac{\partial \bar{\rho} \widetilde{Y_c''^2}}{\partial t} + \frac{\partial \bar{\rho} \bar{u}_j \widetilde{Y_c''^2}}{\partial x_j} &= \frac{\partial}{\partial x_j} \left(\bar{\rho} D \frac{\partial \widetilde{Y_c''^2}}{\partial x_j} - \Phi_{Y_c,v,j} \right) - 2\bar{\rho} \tilde{s}_{\chi_{Y_c}} - 2\Phi_{Y_c,j} \frac{\partial \widetilde{Y_c}}{\partial x_j} \\ &\quad + 2 \left(\overline{Y_c \dot{\omega}_{Y_c}} - \widetilde{Y_c} \bar{\omega}_{Y_c} \right) \end{aligned} \quad (6.67)$$

The terms $\Phi_{Y_c,v,j}$ and $\Phi_{Y_c,j}$ are explained in Table 6.1. The scalar dissipation rate has been decomposed into its resolved and SGS ($\bar{\rho} \tilde{s}_{\chi_{Y_c}}$) parts in LES, or laminar and turbulent part in RANS.

$$\underbrace{\bar{\rho} \tilde{\chi}_{Y_c}}_{\text{scalar dissipation rate}} = \overline{\rho D \left(\frac{\partial Y_c}{\partial x_j} \right)^2} = \underbrace{\bar{\rho} D \left(\frac{\partial \widetilde{Y_c}}{\partial x_j} \right)^2}_{\text{resolved / laminar part}} + \underbrace{\bar{\rho} \tilde{s}_{\chi_{Y_c}}}_{\text{SGS / turbulent part}} \quad (6.68)$$

Transport equation for mixture fraction variance Eq.(6.29) can be obtained following similar procedure.

REFERENCES

- [1] R. L. Gordon, A. R. Masri, S. B. Pope, and G. M. Goldin, *Transport budgets in turbulent lifted flames of methane autoigniting in a vitiated co-flow*, *Combustion and Flame* **151**, 495 (2007).
- [2] C. S. Yoo, E. S. Richardson, R. Sankaran, and J. H. Chen, *A DNS study on the stabilization mechanism of a turbulent lifted ethylene jet flame in highly-heated coflow*, *Proceedings of the Combustion Institute* **33**, 1619 (2011).
- [3] W. O'Loughlin and A. R. Masri, *The Structure of the Auto-Ignition Region of Turbulent Dilute Methanol Sprays Issuing in a Vitiated Co-flow*, *Flow, Turbulence and Combustion* **89**, 13 (2012).
- [4] S. Bhattacharjee and D. C. Haworth, *Simulations of transient n-heptane and n-dodecane spray flames under engine-relevant conditions using a transported PDF method*, *Combustion and Flame* **160**, 2083 (2013).
- [5] S. B. Pope, *Small scales, many species and the manifold challenges of turbulent combustion*, *Proceedings of the Combustion Institute* **34**, 1 (2013).
- [6] J. A. van Oijen and L. P. H. de Goey, *Modelling of premixed laminar flames using flamelet-generated manifolds*, *Combustion Science and Technology* **161**, 113 (2000).
- [7] N. Peters, *Laminar diffusion flamelet models in non-premixed turbulent combustion*, *Progress in Energy and Combustion Science* **10**, 319 (1984).
- [8] A. Rittler, F. Proch, and A. M. Kempf, *LES of the Sydney piloted spray flame series with the PFGM/ATF approach and different sub-filter models*, *Combustion and Flame* **162**, 1575 (2015).
- [9] D. Haworth, *Progress in probability density function methods for turbulent reacting flows*, *Progress in Energy and Combustion Science* **36**, 168 (2010).
- [10] L. Ma, B. Naud, and D. Roekaerts, *Transported PDF Modeling of Ethanol Spray in Hot-diluted Coflow Flame*, *Flow, Turbulence and Combustion*, in press (2015).
- [11] A. Vreman, B. Albrecht, J. A. van Oijen, L. P. H. de Goey, and R. Bastiaans, *Premixed and nonpremixed generated manifolds in large-eddy simulation of Sandia flame D and F*, *Combustion and Flame* **153**, 394 (2008).
- [12] M. Ihme and Y. C. See, *Prediction of autoignition in a lifted methane/air flame using an unsteady flamelet/progress variable model*, *Combustion and Flame* **157**, 1850 (2010).
- [13] R. Cabra, J. Chen, R. Dibble, A. Karpetis, and R. Barlow, *Lifted methane-air jet flames in a vitiated coflow*, *Combustion and Flame* **143**, 491 (2005).
- [14] OpenFOAM, *OpenFOAM: The open source CFD Toolbox*, (2015).